One-dimensional electric field structure of an outer gap accelerator – III. Location of the gap and the gamma-ray spectrum

Kouichi Hirotani[1]★ and Shinpei Shibata[2]★

[1]*National Astronomical Observatory, Osawa, Mitaka, Tokyo 181-8588, Japan*
[2]*Department of Physics, Yamagata University, Yamagata 990-8560, Japan*

ABSTRACT

We investigate a stationary particle acceleration zone in the outer magnetosphere of an obliquely rotating neutron star. The charge depletion as a result of global current causes a large electric field along the magnetic field lines. Migratory electrons and/or positrons are accelerated by this field to radiate curvature gamma-rays, some of which collide with the X-rays to materialize as pairs in the gap. As a result of this pair-production cascade, the replenished charges partially screen the electric field, which is self-consistently solved together with the distribution of particles and gamma-rays. If no current is injected at either of the boundaries of the accelerator, the gap is located around the so-called null surface, where the local Goldreich–Julian charge density vanishes. However, we find that the gap position shifts outwards (or inwards) when particles are injected at the inner (or outer) boundary. We apply the theory to the seven pulsars whose X-ray fields are known from observations. We show that the gap should be located near to or outside of the null surface for the Vela pulsar and PSR B1951+32, so that their expected GeV spectrum may be consistent with observations. We then demonstrate that the intrinsically large TeV flux from the outer gap of PSR B0540–69 is absorbed by the magnetospheric infrared photons, causing it to be undetectable. We also point out that the electrodynamic structure and the resultant GeV emission properties of millisecond pulsars are similar to young pulsars.

Key words: pulsars: individual: B0540−69 – pulsars: individual: B1509−58 – pulsars: individual: B1951+32 – pulsars: individual: Vela – gamma-rays: observation – gamma-rays: theory.

1 INTRODUCTION

The EGRET experiment on the *Compton Gamma Ray Observatory* (*CGRO*) has detected pulsed signals from seven rotation-powered pulsars (for Crab, see Nolan et al. 1993 and Fierro et al. 1998; for Vela, see Kanbach et al. 1994 and Fierro et al. 1998; for Geminga, see Mayer-Hasselwander et al. 1994 or Fierro et al. 1998; for PSR B1706–44, Thompson et al. 1996; for PSR B1046–58, Kaspi et al. 2000; for PSR B1055–52, Thompson et al. 1999; for PSR B1951+32, Ramanamurthy et al. 1995). The modulation of the γ-ray light curves at GeV energies testifies to the production of γ-ray radiation in the pulsar magnetospheres, either at the polar cap (Harding, Tademaru & Esposito 1978; Daugherty & Harding 1982, 1996; Dermer & Sturner 1994; Sturner, Dermer & Michel 1995; Shibata, Miyazaki & Takahara 1998), or at the vacuum gaps in the outer magnetosphere (Cheng, Ho & Ruderman 1986a,b, hereafter CHR; Chiang & Romani 1992, 1994; Romani & Yadigaroglu

1995; Romani 1996; Zhang & Cheng 1997, hereafter ZC97; Cheng, Ruderman & Zhang 2000). Effective γ-ray production in a pulsar magnetosphere may be extended to the very high energy (VHE) region above 100 GeV as well; however, the predictions of fluxes by the current models of γ-ray pulsars are not sufficiently conclusive (e.g. Cheng 1994). Whether or not the spectra of γ-ray pulsars continue up to the VHE region is a question that remains one of the interesting issues of high-energy astrophysics.

In the VHE region, positive detections of radiation at a high-confidence level have been reported from the direction of the Crab, B1706–44, and Vela pulsars (Nel et al. 1993; Edwards et al. 1994; Yoshikoshi et al. 1997; see also Kifune 1996 for a review), by virtue of the technique of imaging Cerenkov light from extensive air showers. However, as for *pulsed* TeV radiation, only the upper limits have been, as a rule, obtained from these pulsars. If the VHE emission originates in the pulsar magnetosphere, rather than the extended nebula, a significant fraction of the flux can be expected to show pulsation. Therefore, the lack of *pulsed* TeV emissions provides a severe constraint on the modelling of particle acceleration zones in a pulsar magnetosphere.

★E-mail: hirotani@milkyway.gsfc.nasa.gov; shibata@sci.kj.yamagata-u.ac.jp

In fact, in the CHR picture, the magnetosphere should be optically thick for pair production in order to reduce the TeV flux to an unobserved level through absorption. This in turn requires very high luminosities of tertiary photons in the infrared energy range. However, the required fluxes are generally orders of magnitude larger than the observed values (Usov 1994). We are therefore motivated by the need to contrive an outer–gap model that produces less TeV emission with a moderate infrared luminosity.

High-energy emission from a pulsar magnetosphere, in fact, crucially depends on the acceleration electric field, $E_\parallel$, along the magnetic field lines. It was Hirotani & Shibata (1999a,b,c; hereafter Papers I, II, and HS99), and Hirotani (2000a,b,c; hereafter H00a, H00b, H00c) who first solved the spatial distribution of $E_\parallel$ together with particle and γ-ray distribution functions. They considered a pair-production cascade in a neutron star magnetosphere by solving the following Vlasov equations (see also Beskin, Istomin & Par'ev 1992 for the original idea applied to black hole magnetospheres):

(i) a Poisson equation describing $E_\parallel$, which accelerate particles ($e^\pm$'s),

(ii) Boltzmann equations of the $e^\pm$'s produced in the gap,

(iii) Boltzmann equations of the γ-rays emitted by the accelerated $e^\pm$'s; some of them collide with the X-rays to materialize as pairs in (ii), which partially screen the original $E_\parallel$ in equation (i).

In this treatment, the X-ray density illuminating the gap is inferred from the observed fluxes and is used to compute the particle-production rate appearing as the source term in equation (ii). The X-ray field of a rotation-powered neutron star within the light cylinder can be attributed to the following three emission processes.

(1) Photospheric emission from the whole surface of a cooling neutron star (Greenstein & Hartke 1983; Romani 1987; Shibanov et al. 1992; Pavlov et al. 1994; Zavlin et al. 1995a).

(2) Thermal emission from the neutron star's polar caps that are heated by the bombardment of relativistic particles streaming back to the surface from the magnetosphere (Kundt & Schaaf 1993; Zavlin, Shibanov, & Pavlov 1995b; Gil & Krawczyk 1996).

(3) Non-thermal emission from relativistic particles accelerated in the pulsar magnetosphere (Ochelkov & Usov 1980a,b; El-Gowhari & Arponen 1972; Aschenbach & Brinkmann 1975; Hardee & Rose 1974; Daishido 1975).

By considering these three X-ray components, they investigated the above-mentioned Vlasov equations, and explicitly solved in Papers I, II and HS99, and H00c the gap width along the field lines, $E_\parallel$, particle densities, and the γ-ray distribution functions. They further demonstrated that a stationary gap is formed around the null surface at which the local Goldreich–Julian charge density,

$$\rho_{GJ} = \frac{\Omega B_z}{2\pi c},\qquad(1)$$

vanishes (Fig. 1), where B_z is the component of the magnetic field along the rotation axis, Ω refers to the angular frequency of the neutron star, and c is the speed of light. Equation (1) is valid unless the gap is located close to the light cylinder, the distance of which from the rotation axis is given by

$$\varpi_{LC} = 3 \times 10^8 \Omega_2^{-1}\ \text{cm},\qquad(2)$$

where $\Omega_2 \equiv \Omega/(100\ \text{rad s}^{-1})$. In this paper, we develop the method presented in H00c as follows.
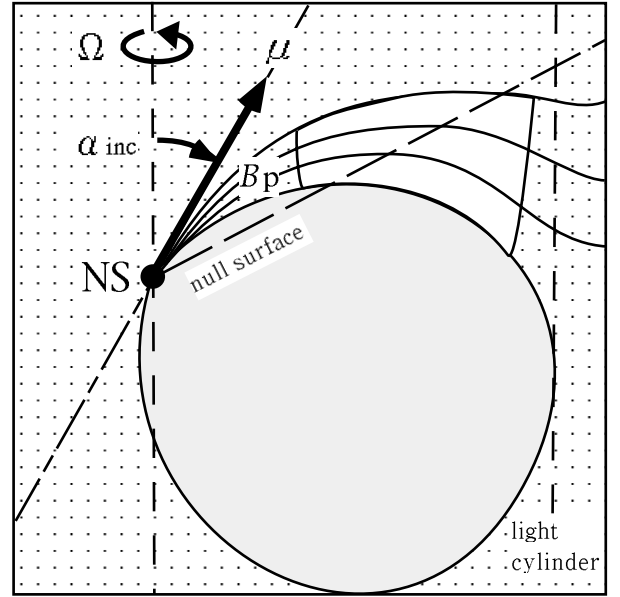
Figure 1. Side view of a hypothetical outer-magnetospheric gap. On the null surface, the Goldreich–Julian charge density vanishes.

(i) We compute the curvature radius, R_C, at each point along the magnetic field line, rather than assuming $R_C = 0.5 \varpi_{LC}$ throughout the gap.

(ii) We partially take the effect of the unsaturated particles into account (equation 43).

(iii) We investigate the gap structure when particles flow into the gap from the inner or the outer boundaries.

(iv) We compute the explicit spectra of TeV emission caused by inverse Compton scatterings, rather than estimating only their upper limits.

In the next two sections, we describe the physical processes of pair production cascade in the outer magnetosphere of a pulsar. We then apply the theory to individual pulsars and we present the expected GeV and TeV spectra for various boundary conditions on the current densities in Section 4. In the final section, we compare the results with previous works.

2 BASIC EQUATIONS AND BOUNDARY CONDITIONS

We first reduce the Poisson equation for the electric potential into a one-dimensional form in Section 2.1. We then give the Boltzmann equations of the particles and the γ-rays in Sections 2.2 and 2.3, and describe the Lorentz factors and the X-ray fields in Sections 2.4 and 2.5. We finally impose suitable boundary conditions in Section 2.6.

2.1 Reduction of the Poisson equation

In the Poisson equation for the electrostatic potential Ψ, the special relativistic effects appear in the higher orders of $(\Omega \varpi/c)^2$, where ϖ indicates the distance of the point from the rotational axis (Shibata 1995). As it is the first-order approximation, we neglect such a term. To simplify the geometry, we further introduce a rectilinear approximation. Unless the gap width, W, along the field lines becomes a good fraction of ϖ_{LC}, we can approximate the magnetic field lines as straight lines parallel to the s-axis (Fig. 2). Here, s is an outwardly increasing coordinate along a magnetic field line,
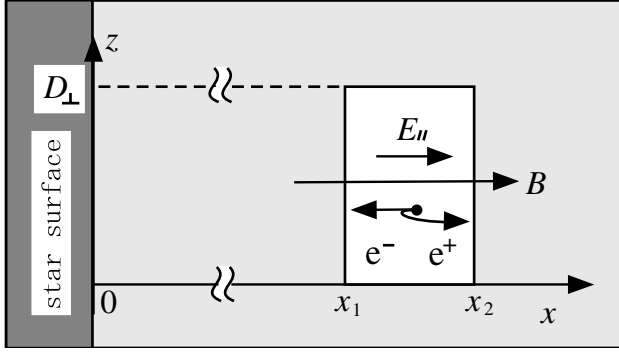
Figure 2. Rectilinear approximation to the outer gap. The *y*-axis, which designates the azimuth, is not depicted to avoid complication. This approximation is valid unless the gap width, $W = s_2 - s_1$, becomes a good fraction of ϖ_{LC}.

while *y* designates the azimuth. Assuming that the typical transfield thickness of the gap, $D_\perp$, is greater than W, we can take the lowest order of Fourier components and replace the transfield derivative of Ψ with $i\Psi/D_\perp$ (Michel 1974). We can then write down the Poisson equation (equation 3 in H00c) into the form

$$-\frac{d^2}{ds^2}\Psi = -\frac{\Psi}{D_\perp^2} + 4\pi e\left(N_+ - N_- - \frac{\rho_{GJ}}{e}\right), \qquad (3)$$

where N_+ and N_- refer to the positronic and electronic densities, respectively, *e* refers to the magnitude of the charge on the electron, and *s* the length along the last-open field line. The left-hand side and the first term on the right-hand side come from the Laplacian of Ψ. The $N_+ - N_-$ term in the parentheses comes from the real charge density, whereas ρ_{GJ} arises from the rotation of the magnetosphere. In what follows, we define the origin of *s* as the neutron star surface.

It is convenient to non-dimensionalize the length scales by a typical Debye scalelength c/ω_p, where

$$\omega_p = \sqrt{\frac{4\pi e^2}{m_e}\frac{\Omega B_{cnt}}{2\pi ce}} = 1.875\times 10^7\Omega_2^{1/2}B_5^{1/2}\text{ rad s}^{-1}; \qquad (4)$$

B_5 represents the magnetic field strength at the gap center in units of 10^5 G. The dimensionless coordinate variable then becomes

$$\xi \equiv (\omega_p/c)s = 6.25\times 10^{-4}\Omega_2^{1/2}B_5^{1/2}s. \qquad (5)$$

By using such dimensionless quantities, we can rewrite the Poisson equation as

$$E_\parallel = -\frac{d\varphi}{d\xi}, \qquad (6)$$

$$\frac{dE_\parallel}{d\xi} = -\frac{\varphi}{\Delta_\perp^2} + \frac{B(\xi)}{B_{cnt}}[n_+(\xi) - n_-(\xi)] + \frac{B_z(\xi)}{B_{cnt}} \qquad (7)$$

where $\Delta_\perp \equiv (\omega_p/c)D_\perp$ and $\varphi(\xi) \equiv e\Psi(s)/(m_ec^2)$; the particle densities are normalized in terms of a typical value of the Goldreich–Julian density as

$$n_\pm(\xi) \equiv \frac{2\pi ce}{\Omega}\frac{N_\pm(s)}{B(s)}. \qquad (8)$$

$B_{cnt} \equiv B(\xi_{cnt})$ refers to the magnetic field strength at the gap center, $\xi = \xi_{cnt}$. In the non-relativistic limit, the local Goldreich–Julian

charge density is given by

$$\frac{B_z(\xi)}{B_{cnt}} = \frac{2\cos\theta\cos(\theta - \alpha_i) - \sin\theta\sin(\theta - \alpha_i)}{\sqrt{1 + 3\cos^2(\theta_{cnt} - \alpha_i)}}, \qquad (9)$$

where α_i refers to the inclination angle of the magnetic moment, θ the colatitude angle with respect to the rotational axis at the position where ρ_{GJ} is measured, and θ_{cnt} is the same colatitude angle at the gap centre. Neglecting the general relativistic effect near to the star surface, we can implicitly solve θ in terms of *s* from

$$\frac{s}{\varpi_{LC}} = \int_{\theta_*}^\theta \frac{\sin(\theta - \alpha_i)\sqrt{1 + 3\cos^2(\theta - \alpha_i)}}{\sin\theta_{LC}\sin^2(\theta_{LC} - \alpha_i)}d\theta, \qquad (10)$$

where θ_* is the colatitude angle of the last-open field line at the star surface; it is given by

$$\frac{\sin^2(\theta_* - \alpha_i)}{r_*} = \frac{\sin^2(\theta_{LC} - \alpha_i)}{\varpi_{LC}/\sin\theta_{LC}}, \qquad (11)$$

where r_* refers to the neutron-star radius, and θ_{LC} the colatitude angle of the intersection of the last-open field line and the light cylinder. We can solve θ_{LC} for a given α_i from

$$2\cot(\theta_{LC} - \alpha_i)\sin\theta_{LC} + \cos\theta_{LC} = 0. \qquad (12)$$

Equations (9)–(12) are valid for a Newtonian dipole field. Therefore, we must pay attention that this Newtonian dipole approximation breaks down if the gap is located close to the light cylinder.

2.2 Particle continuity equations

Let us now consider the continuity equations of the particles. It should be noted that almost all the particles migrate with the large, saturated Lorentz factor, defined by the mutual cancellation of the electric acceleration and the curvature-radiation reaction. We therefore assume here that both electrostatic and curvature-radiation reaction forces cancel out each other. Then the spatial number density of the outwardly and inwardly propagating particles, $N_+(s)$ and $N_-(s)$, at distance *s* from the neutron-star surface along the last-open field line, obey the following continuity equations:

$$\frac{\partial N_\pm}{\partial t} + \boldsymbol{v}\cdot\frac{\partial N_\pm}{\partial \boldsymbol{x}} = Q(x), \qquad (13)$$

where

$$Q(x) \equiv \frac{1}{c}\int_0^\infty d\epsilon_\gamma[\eta_{p+}G_+ + \eta_{p-}G_-]; \qquad (14)$$

$G_+(s, \epsilon_\gamma)$ and $G_-(s, \epsilon_\gamma)$ refer to the distribution functions of outwardly and inwardly propagating γ-ray photons, respectively, having energy $m_ec^2\epsilon_\gamma$. For charge definiteness, we consider that a positive electric field arises in the gap. In this case, N_+ (or N_-) represents the number densities of positrons (or electrons).

The particle velocity at position (r, θ) becomes (equation 21 in H00c)

$$\boldsymbol{v} = \boldsymbol{v}_p + \left(r\Omega\sin\theta + \kappa B_\phi - cE_\parallel\frac{B_\phi}{B^2}\right)\boldsymbol{e}_\phi, \qquad (15)$$

where κ is a constant and $\boldsymbol{e}_\phi$ refer to the azimuthal unit vector. In the parentheses, the term $r\Omega\sin\theta$ is caused by corotation, while κB_ϕ is caused by magnetic bending. As $E_\parallel$ arises in the gap, the corresponding drift velocity appears as $-cE_\parallel B_\phi/B^2$. Unless the gap is located close to the light cylinder, we can neglect the terms

containing B_ϕ as a first-order approximation. We thus have

$$\boldsymbol{v} \approx \boldsymbol{v}_{\mathrm{p}} + r\Omega \sin\theta \boldsymbol{e}_\phi. \tag{16}$$

Imposing a stationarity condition,

$$[\partial_t + (r\Omega \sin\theta)\partial_\phi]N_\pm = 0, \tag{17}$$

remembering that the projected velocity on the poloidal plane is $\boldsymbol{v}_{\mathrm{p}} = c\cos\Phi\boldsymbol{B}_{\mathrm{p}}$, and utilizing $\mathrm{div}\boldsymbol{B}_{\mathrm{p}} \approx \mathrm{div}\boldsymbol{B} = 0$, we obtain

$$\pm B \frac{\mathrm{d}}{\mathrm{d}s}\left(\frac{N_\pm}{B}\right) = \frac{1}{c\cos\Phi}\int_0^\infty \mathrm{d}\epsilon_\gamma [\eta_{\mathrm{p}+} G_+ + \eta_{\mathrm{p}-} G_-]. \tag{18}$$

Φ refers to the projection angle of the particle three-dimensional motion onto the poloidal plane and is evaluated at the gap centre (at distance r_{cnt} from the star centre) as $\Phi = \arcsin(r_{\mathrm{cnt}}\Omega\sin\theta/\varpi_{\mathrm{LC}})$. The left-hand side represents the divergence of the particle flux, while the right-hand side is the particle creation rate per unit length. Since the electric field is assumed to be positive in the gap, e^+s (or e^-s) migrate outwards (or inwards). The pair production redistribution functions for outwardly (or inwardly) propagating γ-rays are written as $\eta_{\mathrm{p}+}$ (or $\eta_{\mathrm{p}-}$), where

$$\eta_{\mathrm{p}\pm}(\epsilon_\gamma) = (1 - \mu_{\mathrm{c}})\frac{c}{\omega_{\mathrm{p}}}\int_{\epsilon_{\mathrm{th}}}^\infty \mathrm{d}\epsilon_{\mathrm{x}}\frac{\mathrm{d}N_{\mathrm{x}}}{\mathrm{d}\epsilon_{\mathrm{x}}}\sigma_{\mathrm{p}}(\epsilon_\gamma, \epsilon_{\mathrm{x}}, \mu_{\mathrm{c}}), \tag{19}$$

where σ_{p} is the pair-production cross-section and $\cos^{-1}\mu_{\mathrm{c}}$ refers to the collision angle between outwardly (or inwardly) propagating γ-rays and the X-ray photon with energy $m_{\mathrm{e}}c^2\epsilon_{\mathrm{x}}$; the X-ray number density between dimensionless energies ϵ_{x} and $\epsilon_{\mathrm{x}} + \mathrm{d}\epsilon_{\mathrm{x}}$ is integrated over ϵ_{x} from the threshold energy $\epsilon_{\mathrm{th}} \equiv 2(1 - \mu_{\mathrm{c}})^{-1}\epsilon_\gamma^{-1}$ to infinity. The explicit expression of σ_{p} is given by (Berestetskii et al. 1989)

$$\sigma_{\mathrm{p}}(\epsilon_\gamma, \epsilon_{\mathrm{x}}, \mu_{\mathrm{c}}) \equiv \frac{3}{16}\sigma_{\mathrm{T}}(1 - v^2)\left[(3 - v^4)\ln\frac{1 + v}{1 - v} - 2v(2 - v^2)\right],$$

$$v(\epsilon_\gamma, \epsilon_{\mathrm{x}}, \mu_{\mathrm{c}}) \equiv \sqrt{1 - \frac{2}{1 - \mu_{\mathrm{c}}}\frac{1}{\epsilon_\gamma\epsilon_{\mathrm{x}}}}, \tag{20}$$

where σ_{T} is the Thomson cross-section, and $\epsilon_{\mathrm{x}} \equiv E_{\mathrm{x}}/m_{\mathrm{e}}c^2$ refers to the dimensionless energy of an X-ray photon.

To evaluate μ_{c} between the surface X-rays and the γ-rays, we must consider γ-ray's toroidal momenta due to the aberration of light. It should be noted that a γ-ray photon propagates in the instantaneous direction of the particle motion at the time of the emission. The toroidal velocity of a particle at the gap center $(r_{\mathrm{cnt}}, \theta_{\mathrm{cnt}})$ becomes

$$v_\phi = r_{\mathrm{cnt}}\sin\theta_{\mathrm{cnt}}\Omega + \kappa B_\phi - E_\| B_\phi\frac{c}{B^2}, \tag{21}$$

where κ is a constant. On the right-hand side, the first term is caused by corotation, while second one is caused by magnetic bending. As $E_\|$ arises in the gap, the corresponding drift velocity appears as the third term. Unless the gap is located close to the light cylinder, we can neglect the terms containing B_ϕ as a first-order approximation. We thus have $v_\phi = r_{\mathrm{cnt}}\sin\theta_{\mathrm{cnt}}\Omega$. As the three-dimensional particle velocity is virtually c, the angle between the particle motion and the poloidal plane becomes

$$\phi_{\mathrm{ab}} = \sin^{-1}\left(\frac{r_{\mathrm{cnt}}\sin\theta_{\mathrm{cnt}}\Omega}{c}\right) = \sin^{-1}\left(\frac{r_{\mathrm{cnt}}\sin\theta_{\mathrm{cnt}}}{\varpi_{\mathrm{LC}}}\right). \tag{22}$$

We evaluate $(r_{\mathrm{cnt}}, \theta_{\mathrm{cnt}})$ along a Newtonian dipole. Using ϕ_{ab}, we can compute μ_{c} as

$$\mu_{\mathrm{c}} = \cos\phi_{\mathrm{ab}}\cos\theta_{\mathrm{pol}}, \tag{23}$$

where θ_{pol} is the collision angle between the surface X-rays and the curvature γ-rays, that is, the angle between the two vectors $(r_{\mathrm{cnt}}, \theta_{\mathrm{cnt}})$ and (B^r, B^θ) at the gap centre. Therefore, the collision approaches head-on (or tail-on) for inwardly (or outwardly) propagating γ-rays, as the gap shifts towards the star.

For magnetospheric, power-law X-rays, we assume

$$\mu_{\mathrm{c}} = \cos(W/\varpi_{\mathrm{LC}}) \tag{24}$$

for both inwardly and outwardly propagating γ-rays. Aberration of light is not important for this component, because both the X-rays and the γ-rays are emitted nearly at the same place, provided that $W \ll \varpi_{\mathrm{LC}}$ holds.

Let us introduce the following dimensionless γ-ray densities in the dimensionless energy interval between β_{i-1} and β_i, such that

$$g_\pm^i(\xi) \equiv \frac{2\pi ce}{\Omega B_{\mathrm{cnt}}}\int_{\beta_{i-1}}^{\beta_i}\mathrm{d}\epsilon_\gamma G_\pm(s, \epsilon_\gamma). \tag{25}$$

In this paper, we set $\beta_0 = 10^2$; this implies that the lowest γ-ray energy considered is $m_{\mathrm{e}}c^2 = 51.1\,\mathrm{MeV}$. To cover a wide range of γ-ray energies, we divide the γ-ray spectra into nine energy bins and put $\beta_1 = 3.162 \times 10^2$, $\beta_2 = 10^3$, $\beta_3 = 3.162 \times 10^3$, $\beta_4 = 10^4$, $\beta_5 = 3.162 \times 10^4$, $\beta_6 = 5.623 \times 10^4$, $\beta_7 = 10^5$, $\beta_8 = 1.778 \times 10^5$ and $\beta_9 = 3.162 \times 10^5$.

We can now rewrite equation (18) in the dimensionless form,

$$\frac{\mathrm{d}n_\pm}{\mathrm{d}\xi} = \pm\frac{B_{\mathrm{cnt}}}{B(\xi)\cos\Phi}\sum_{i=1}^9 [\eta_{\mathrm{p}+}^i g_+^i(\xi) + \eta_{\mathrm{p}-}^i g_-^i(\xi)], \tag{26}$$

where $\eta_{\mathrm{p}\pm}^i$ are evaluated at the central energy in each bin as

$$\eta_{\mathrm{p}\pm}^i \equiv \frac{1}{\omega_{\mathrm{p}}}\eta_{\mathrm{p}\pm}\left(\frac{\beta_{i-1} + \beta_i}{2}\right). \tag{27}$$

A combination of equations (26) for positrons and electrons gives the current conservation law,

$$j_{\mathrm{tot}} \equiv n_+(\xi) + n_-(\xi) = \text{ constant for } \xi. \tag{28}$$

When $j_{\mathrm{tot}} = 1.0$, the current density per unit flux tube equals the Goldreich–Julian value, $\Omega/(2\pi)$.

2.3 Gamma-ray Boltzmann equations

Let us next consider the γ-ray Boltzmann equations. The γ-rays are beamed in the direction of the magnetic field where they were emitted. Therefore, the propagation direction of each γ-ray photon does not coincide with the local magnetic field where the γ-ray distribution is evaluated. However, to avoid complications, we simply assume that the outwardly (or inwardly) propagating γ-rays dilate (or constrict) at the same rate with the magnetic field (Hirotani & Shibata 2001, hereafter HS01). Then we can write down the γ-ray Boltzmann equations into the form

$$\pm B\frac{\partial}{\partial s}\left[\frac{1}{B}G_\pm(s, \epsilon_\gamma)\right] = \frac{-\eta_{\mathrm{p}\pm}G_\pm(s, \epsilon_\gamma) + \eta_{\mathrm{c}}N_\pm(s)}{c\cos\Phi}, \tag{29}$$

where (e.g., Rybicki & Lightman 1979)

$$\eta_{\mathrm{c}} \equiv \frac{\sqrt{3}e^2\Gamma}{hR_{\mathrm{C}}}\frac{1}{\epsilon_\gamma}F\left(\frac{\epsilon_\gamma}{\epsilon_{\mathrm{c}}}\right), \tag{30}$$

$$\epsilon_{\mathrm{c}} \equiv \frac{1}{m_{\mathrm{e}}c^2}\frac{3}{4\pi}\frac{hc\Gamma^3}{R_{\mathrm{C}}}, \tag{31}$$

$$F(s) \equiv s\int_x^\infty K_{5/3}(t)\,\mathrm{d}t; \tag{32}$$

R_{C} is the curvature radius of the magnetic field lines and $K_{5/3}$ is the

modified Bessel function of the order of 5/3. The left-hand side represents the divergence of the γ-ray flux, while the right-hand side represents the γ-ray production rate per unit length. The effect of the broad spectrum of curvature γ-rays is represented by the factor $F(\epsilon_\gamma/\epsilon_c)$ in equation (30). In the polar coordinates (r, θ), the explicit expression of R_C is given by

$$\frac{R_C}{\varpi_{LC}} = \left| 1 + \left(\frac{d\zeta}{d\xi} \right)^2 \right|^{3/2} \times \left| \frac{d^2\zeta}{d\xi^2} \right|^{-1}, \tag{33}$$

where

$$\zeta \equiv r \cos\theta / \varpi_{LC}, \tag{34}$$

$$\xi \equiv r \sin\theta / \varpi_{LC}. \tag{35}$$

Assuming a Newtonian dipole magnetic field with inclination α_i, we can write the derivatives in equation (33) as

$$\frac{d\zeta}{d\xi} = \frac{\cos\alpha_i - (3/2)\sin\theta\sin(\theta - \alpha_i)}{\sin\alpha_i + (3/2)\cos\theta\sin(\theta - \alpha_i)}, \tag{36}$$

$$\frac{d^2\zeta}{d\xi^2} = \frac{1}{\rho} \frac{(d\zeta/d\xi)f - \sin\theta\cos\alpha_i + (3/2)\cos\theta\sin\alpha_i}{\sin\alpha_i + (3/2)\cos\theta\sin(\theta - \alpha_i)}, \tag{37}$$

where

$$\frac{\sin^2(\theta - \alpha_i)}{\rho} = \frac{\sin^2(\theta_* - \alpha_i)}{r_*/\varpi_{LC}}, \tag{38}$$

$$f \equiv \left(\cos\theta\sin\alpha_i - \frac{3}{2}\sin\theta\cos\alpha_i \right) \frac{d\zeta}{d\xi} + \frac{1}{2}\cos(\theta + \alpha_i). \tag{39}$$

Integrating (29) in the energy intervals $[\beta_{i-1}, \beta_i]$, we obtain

$$\pm \frac{d}{d\xi} g_\pm^i(\xi) = \pm \frac{d}{d\xi}(\ln B)g_\pm^i - \eta_{p\pm}^i g_\pm^i + \eta_c^i \frac{B(\xi)}{B_{cnt}} n_\pm, \tag{40}$$

where $i = 1, 2, \ldots, m$ $(m = 9)$ and

$$\eta_c^i \equiv \frac{\sqrt{3}e^2\Gamma}{\omega_p h R_C} \int_{\beta_{i-1}/\epsilon_c}^{\beta_i/\epsilon_c} du \int_u^\infty K_{\frac{5}{3}}(t)\,dt$$

$$= 2.14 \times 10^{-8} \Gamma \left(\frac{R_C}{0.5\varpi_{LC}} \right)^{-1} \sqrt{\frac{\Omega_2}{B_5}}$$

$$\times \int_{\beta_{i-1}/\epsilon_c}^{\beta_i/\epsilon_c} ds \int_s^\infty K_{5/3}(t)\,dt. \tag{41}$$

2.4 Terminal Lorentz factor

The most effective assumption for particle motion in the gap arises from the fact that the velocity immediately saturates in the balance between the electric force and the radiation reaction force caused by curvature radiation. Equating the electric force $e|d\Psi/ds|$ and the radiation reaction force, we obtain the saturated Lorentz factor at each point,

$$\Gamma_{sat} = \left(\frac{3R_C^2}{2e} \left| \frac{d\Psi}{ds} \right| + 1 \right)^{1/4}. \tag{42}$$

When W is so small that a significant fraction of the particles are unsaturated, equation (42) overestimates the Lorentz factors of the particle. To take account of such unsaturated motion of the

particles, we compute Γ from

$$\frac{1}{\Gamma} = \sqrt{\frac{1}{\Gamma_{sat}^2} + \frac{1}{\varphi^2(\xi_2)}}, \tag{43}$$

where

$$\varphi(\xi_2) = \frac{e\Psi(s_2)}{m_e c^2} \tag{44}$$

represents the maximum attainable Lorentz factor; the gap is considered to exist in $\xi_1 < \xi < \xi_2$ and the potential origin is chosen such that $\varphi(\xi_1) = 0$.

2.5 X-ray field

To execute the integration in equation (19), we must specify the X-ray field illuminating the gap. Let us discuss the details of the three X-ray components (soft-surface blackbody, hard-surface blackbody, and the magnetospheric power-law components) in this subsection.

First, the spectrum of the soft blackbody component is expected to be expressed with a modified blackbody. However, for simplicity, we approximate it in terms of a Plank function with temperature kT_s, because the X-ray spectrum is occasionally fitted by a simple blackbody spectrum. We regard a blackbody component as the first one if its observed emitting area, A_s, is comparable with the whole surface of a neutron star, $A_* \equiv 4\pi r_*^2$, where r_* denotes the neutron star radius. We take account of both the pulsed and the non-pulsed surface blackbody emission for this soft blackbody component. At distance r from the centre of the star, the X-ray density between energies ϵ_x and $\epsilon_x + d\epsilon_x$ is given by the Planck law,

$$\frac{dN_x}{d\epsilon_x} = \frac{1}{4\pi^2} \left(\frac{m_e c^2}{c\hbar} \right)^3 \left(\frac{A_s}{4\pi r^2} \right) \frac{\epsilon_x^2}{\exp(\epsilon_x/\Delta_s) - 1}, \tag{45}$$

where Δ_s is defined by

$$\Delta_s \equiv \frac{kT_s}{m_e c^2}; \tag{46}$$

kT_s refers to the soft blackbody temperature measured by a distant observer. As the outer gap is located outside of the deep gravitational potential well of the neutron star, the photon energy there is essentially the same as what a distant observer measures.

As for the second, hard blackbody component, we regard a blackbody component as the heated polar cap emission if its observed emitting area, A_h, is much smaller than A_*. We approximate its spectrum by a Planck function. We take account of both the pulsed and the non-pulsed polar cap emission for this hard blackbody component. In the same manner as in the soft blackbody case, the spectrum at a radius r becomes

$$\frac{dN_x}{d\epsilon_x} = \frac{1}{4\pi^2} \left(\frac{m_e c^2}{c\hbar} \right)^3 \left(\frac{A_h}{4\pi r^2} \right) \frac{\epsilon_x^2}{\exp(\epsilon_x/\Delta_s) - 1}, \tag{47}$$

where Δ_h is related to the hard blackbody temperature, kT_h, as

$$\Delta_h \equiv \frac{kT_h}{m_e c^2}. \tag{48}$$

Unlike the first and the second components, a power-law component is usually dominated by a nebula emission. To get rid of the nebula emission, which illuminates the outer gap inefficiently, we adopt only the pulsed components of a power-law emission as

the third component. We describe a magnetospheric component with the power law,

$$\frac{dN_{pl}}{d\epsilon_x} = N_{pl}\epsilon_x^{\alpha} \quad (\epsilon_{min} < \epsilon_x < \epsilon_{max}). \tag{49}$$

The photon index α is typically between -2 and -1 for a pulsed, power-law X-ray component in hard X-ray band (e.g. Saito 1998). We assume $\epsilon_{min} = 0.1/511\,\mathrm{keV}$ and $\epsilon_{max} = 50/511\,\mathrm{keV}$ for homogeneous discussion.

2.6 Boundary conditions

To solve the Vlasov equations (6), (7), (26), and (40), we must impose boundary conditions. The inner boundary is defined so that $E_\parallel$ vanishes there. Therefore, we have

$$E_\parallel(\xi_1) = 0. \tag{50}$$

It is noteworthy that condition (50) is consistent with the stability condition at the plasma–vacuum interface (Krause-Polstorff & Michel 1985a,b). At the inner (starward) boundary ($\xi = \xi_1$), we impose (H00a)

$$\varphi(\xi_1) = 0, \tag{51}$$

from a convention and

$$g_+^i(\xi_1) = 0 \quad (i = 1, 2, \ldots, m), \tag{52}$$

where $m = 9$, by assuming that γ-rays do not penetrate into the gap across the boundary. Unlike the γ-rays, particles flow along the field lines outside of the gap, by virtue of the residual electric field that causes the global current pattern. Therefore, the created particles outside the gap (because of the collisions of photons) are allowed to flow into the gap across the boundaries. At the inner boundary, positrons flow into the gap. We parameterize such a positronic current injection per unit magnetic flux tube, by dividing it with ce as follows:

$$n_+(\xi_1) = j_1. \tag{53}$$

This yields, with the help of the charge-conservation law (equation 28),

$$n_-(\xi_1) = j_{tot} - j_1. \tag{54}$$

At the outer boundary ($\xi = \xi_2$), we impose

$$E_\parallel(\xi_2) = 0, \tag{55}$$

$$g_-^i(\xi_2) = 0 \quad (i = 1, 2, \ldots, m), \tag{56}$$

$$n_-(\xi_2) = j_2. \tag{57}$$

The current (divided by ce) created in the gap per unit flux tube can be expressed as

$$j_{gap} = j_{tot} - j_1 - j_2. \tag{58}$$

We adopt j_{gap}, j_1 and j_2 as the free parameters in this paper.

We have total $2m + 6$ boundary conditions (50)–(57) for $2m + 4$ unknown functions Ψ, $E_\parallel$, n_+, n_-, g_+^1, g_+^2, ..., g_+^m, g_-^1, g_-^2, ..., g_-^m. Thus two extra boundary conditions must be compensated by making the positions of the boundaries ξ_1 and ξ_2 free. The two free boundaries appear because $E_\parallel = 0$ is imposed at *both* the boundaries and because j_{gap} is externally imposed. In other words, the gap boundaries (ξ_1 and ξ_2), and hence the positions shift if j_1 and/or j_2 varies.

3 TEV SPECTRA

In TeV energies, inverse Compton (IC) scatterings of infrared (IR) photons off relativistic electrons and positrons ($\Gamma \sim 10^7$) are the process of γ-ray production. We briefly discuss the IR field in Section 3.1, and describe the intrinsic TeV emission from the gap in Section 3.2 and the extrinsic absorption due to magnetospheric IR field in Section 3.3.

3.1 Infrared photon field

Without a careful consideration of the synchrotron beaming, it is difficult to estimate the specific intensity of the IR field. Therefore, we simply assume that the IR field is homogeneous and isotropic within the radius ϖ_{LC}. This assumption comes from the following emission scenario in the magnetosphere: The primary γ-rays emitted in the gap collide with X-ray and IR photons outside of the gap to materialize as primary pairs, which emit secondary photons in X-ray and soft γ-ray energies via a synchrotron process. Some portions of the secondary photons collide with each other to materialize as tertiary pairs in the magnetosphere. The tertiary pairs have much lower energies compared with the secondary pairs and emit copious tertiary IR photons via a synchrotron process. On these grounds, we may expect that the tertiary IR field has lost the directional information of the primary γ-rays, compared with the secondary X-ray field.

We do not adopt a broken power law to describe the soft photons from IR to X-ray energies. This is because the adopted assumptions are different from each other. As described in Section 2.5, we assume that the secondary, power-law X-ray field is homogeneous only within the radius of r_{cnt} around the gap and is highly beamed along the magnetic field at the gap centre, so that the collision angles between the primary γ-rays and the secondary X-rays in the gap are typically W/ϖ_{LC} radian (equation 24). On the other hand, we assume that the tertiary, power-law IR field is homogeneous and isotropic within the radius ϖ_{LC}.

At distance r from the centre of the star, we adopt the following power-law IR spectra:

$$\frac{dN_{IR}}{d\epsilon_{IR}} = N_{IR}\left(\frac{d}{\mathrm{kpc}}\right)^2\left(\frac{r}{\varpi_{LC}}\right)^{-2}\epsilon_{IR}^{\alpha}, \tag{59}$$

where $\epsilon_{IR}m_ec^2$ refers to the IR photon energy, and $\epsilon_{IR,min} < \epsilon < \epsilon_{IR,max}$. We adopt $\epsilon_{IR,min} = 10^{-8}$ and $\epsilon_{IR,max} = 10^{-6}$; the results do not depend on these cut-off energies very much.

3.2 Inverse compton scatterings

When an electron or a positron is migrating with Lorentz factor $\Gamma \gg 1$ in an isotropic photon field, it upscatters the soft photons to produce the following number spectrum of γ-rays (Blumenthal & Gould 1970):

$$\frac{d^2N}{dt\,d\epsilon_\gamma} = \frac{3}{4}\sigma_T\frac{c}{\Gamma^2}\frac{dN_{IR}}{d\epsilon_{IR}}\frac{d\epsilon_{IR}}{\epsilon_{IR}}$$
$$\times\left[2q\ln q + (1 + 2q)(1 - q) + \frac{(Qq)^2(1 - q)}{2(1 + Qq)}\right], \tag{60}$$

where $Q \equiv 4\epsilon_{IR}\Gamma$ and $q \equiv \epsilon_\gamma/Q(\Gamma - \epsilon_\gamma)$; here, ϵ_γ refers to the energy of the upscattered photons in units of m_ec^2. Substituting equation (59), integrating $d^2N/dt\,d\epsilon_\gamma$ over ϵ_{IR}, and multiplying the γ-ray energy ($\epsilon_\gamma m_ec^2$) and the electron number (N_e) in the gap, we

obtain the flux density of the upscattered photons as a function of ϵ_γ.

3.3 Absorption caused by pair production

As mentioned in Section 3.1, the IR field is assumed to be homogeneous and isotropic within radius ϖ_{LC}. Outside of ϖ_{LC}, both the IR photon density and the collision angles decrease; therefore, we neglect the pair production at $r > \varpi_{LC}$ for simplicity. The optical depth then becomes

$$\tau(\epsilon_\gamma) = L \int_{\epsilon_{IR,min}}^{\epsilon_{IR,max}} \frac{dN_{IR}}{d\epsilon_{IR}} \sigma_p(\epsilon_{IR}, \epsilon_\gamma, \mu_c) \, d\epsilon_{IR}, \tag{61}$$

where L refers to the path length. For homogeneous discussion, we assume $L = 0.5\varpi_{LC}$ in this paper. As the first order approximation, we adopt $90°$ as the collision angles in the isotropic IR field to substitute $\mu_c = 0$ in equation (61), where σ_p is defined by equation (20).

4 APPLICATION TO INDIVIDUAL PULSARS

In this section, we apply the theory to the seven rotation-powered pulsars whose X-ray field at the outer gap can be deduced from observations. The Crab pulsar was investigated in detail in HS01; therefore, we exclude this young pulsar in this paper. We first describe their X-ray and infrared fields in the next two subsections, and we present the electric field distribution in Section 4.3 and the resultant GeV and TeV emissions from individual pulsars in Section 4.4.

4.1 Input X-ray field

We present the observed X-ray properties of individual pulsars in order of spin-down luminosity, $\dot{E}_{rot}$ (Table 1).

B0540–69 From *ASCA* observations in the 2–10 keV band, its X-ray radiation is known to be well fitted by a power law with $\alpha = -2.0$. The unabsorbed luminosity in this energy range is $1.3 \times 10^{36} \, \mathrm{erg \, s^{-1}}$, which leads to $N_{pl} = 9.0 \times 10^9 d^2 (r_0/\varpi_{LC})^{-2}$ (Saito 1998), where d is the distance to the pulsar in kpc.

B1509–58 From *ASCA* observations in the 2–10 keV band, its pulsed emission can be fitted by a power law with $\alpha = -1.1$. The unabsorbed flux in this energy range is $2.9 \times 10^{-11} \, \mathrm{erg \, cm^{-2} \, s^{-1}}$, which leads to $N_{pl} = 9.3 \times 10^{11} d^2 (r_0/\varpi_{LC})^{-2}$.

J1617–5055 and **J0822–4300** These two pulsars have similar parameters, such as $\Omega \sim 90 \, \mathrm{rad \, s^{-1}}$, $\mu \sim 10^{30.6} \, \mathrm{G \, cm^3}$, and characteristic age $\sim 8 \times 10^3$ yr. From the *ASCA* observations of J1617–5055 in the 3.5–10 keV band, its pulsed emission subtracted the background and the steady components can be fitted by a power law with $\alpha = -1.6$ (Torii et al. 1998).

Adopting the distance of 3.3 kpc, we can calculate its unabsorbed flux as $3.1 \times 10^{-12} \, \mathrm{erg \, cm^{-2} \, s^{-1}}$, which yields $N_{pl} = 6.5 \times 10^{10} d^2 (r_0/\varpi_{LC})^{-2}$. On the other hand, the distance of J0822–4300 was estimated from VLA observations as $d = 2.2 \pm 0.3$ kpc (Reynoso et al. 1995). *ROSAT* observations revealed that the soft X-ray emission of this pulsar is consistent with a single-temperature blackbody model with $kT_s = 0.28 \pm 0.10$ keV and $A_s \sim 0.04 A_* (d/2.2)^2$ (Petre, Becker & Winkler 1996).

Vela From *ROSAT* observations in 0.06–2.4 keV, the spectrum of its point-source (presumably the pulsar) emission is expressed by two components: surface blackbody component with $kT_s = 150$ eV and $A_s = 0.066 A_* (d/0.5)^2$ and a power-law component with $\alpha = -3.3$ (Oügelman, Finley & Zimmermann 1993). However, the latter component does not show pulsations; therefore, we consider only the former component to be the X-ray field illuminating the outer gap.

B1951+32 From *ROSAT* observations in 0.1–2.4 keV, the spectrum of its point-source (presumably the pulsar) emission can be fitted by a single power-law component with $\alpha = -1.6$ and intrinsic luminosity of $2.3 \times 10^{33} (d/2.5)^2 \, \mathrm{erg \, s^{-1}}$ (Safi-Harb et al. 1995), which yields $N_{pl} = 9.1 \times 10^{11} d^2 (r_0/\varpi_{LC})^{-2}$. The extension of this power law is consistent with the upper limit of the pulsed component in the 2–10 keV energy band (Saito 1998).

J0437–4715 Using *ROSAT* and *EUVE* data (Becker & Truümper 1993; Halpern, Martin & Marshall 1996), Zavlin and Pavlov (1998) demonstrated that both the spectra and the light curves of its soft X-ray radiation can originate from hot polar caps with a non-uniform temperature distribution, and be modelled by step-like functions having two different temperatures. The first component is the emission from heated polar-cap core with temperature $kT_h = 10^{6.16}$ K measured at the surface and with an area $A_h = 5.3 \times 10^{-4} A_* (d/0.180)^2$. The second one can be interpreted as a cooler rim around the polar cap on the neutron star surface with temperature $kT_s = 10^{5.53}$ K and with an area $A_s = 0.16 A_* (d/0.180)^2$. Considering the gravitational redshift factor of 0.76, the best-fitting temperatures observed at infinity become $kT_s = 22$ eV and $kT_h = 95$ eV. From parallax measurements, its distance is reported to be 178 ± 26 pc (Sandhu et al. 1997). We adopt $d = 180$ pc as a representative value.

4.2 Input infrared field

We next consider the homogeneous and isotropic infrared field in the magnetosphere. In addition to the references cited below, see also Thompson et al. (1999).

B0540–69 Its de-extincted optical and soft X-ray pulsed flux densities can be interpolated as $F_\nu = 0.207 \nu^{-0.3}$ Jy (Middleditch & Pennypacker 1985). This line extrapolates to 0.47 mJy at

Table 1. Input X-ray field.

Pulsar	Distance kpc	Ω rad s^{-1}	$\log_{10}\mu$ lg(G cm^3)	kT_s eV	$A_s A_*$	kT_h eV	$A_h A_*$	N_{pl} cm^{-3}	$-\alpha$
B0540–69	49.4	124.7	31.00	…	…	…	…	$10^{14.15}$	2.0
B1509–58	4.40	41.7	31.19	…	…	…	…	$10^{14.04}$	1.1
J1617–5055	3.30	90.6	30.78	…	…	…	…	$10^{12.64}$	1.6
J0822–4300	2.20	83.4	30.53	280	0.040	…	…	…	…
Vela	0.50	61.3	30.53	150	0.066	…	…	…	…
B1951+32	2.5	159	29.68	…	…	…	…	$10^{13.55}$	1.6
J0437–4715	0.180	1092	26.50	22	0.16	95	$10^{-3.28}$	…	…

640 MHz, which is consistent with an observed value of 0.4 mJy (Manchester et al. 1993). We thus extrapolate the relation $F_\nu = 0.207\nu^{-0.3}$ to the infrared energies and obtain (H00b)

$$dN_{IR}/d\epsilon_{IR} = 1.6 \times 10^{12} d^2 \epsilon_{IR}^{-1.3} \tag{62}$$

B1509–58 The flux densities emitted from close to the neutron star in radio (Taylor, Manchester & Lyne 1993), optical (Caraveo, Mereghetti & Bignami 1994), soft X-ray (Seward et al. 1984), and hard X-ray (Kawai et al. 1993) bands can be fitted by a single power law $F_\nu = 1.36\nu^{-0.32}$ Jy. We thus adopt

$$dN_{IR}/d\epsilon_{IR} = 4.7 \times 10^{11} d^2 \epsilon_{IR}^{-1.3} \tag{63}$$

Vela The flux densities emitted from close to the neutron star in radio (Taylor et al. 1993; Downs, Reichley & Morris 1973), optical bands (Manchester et al. 1980) can be fitted by $F_\nu = 1.71 \times 10^7 \nu^{-0.91}$ Jy. We thus adopt

$$dN_{IR}/d\epsilon_{IR} = 1.8 \times 10^7 d^2 \epsilon_{IR}^{-1.9} \tag{64}$$

B1951 + 32, The flux densities emitted from close to the neutron star in radio (Taylor et al. 1993) and soft X-ray (Safi-Harb et al. 1995) bands can be interpolated as $F_\nu = 32.8\nu^{-0.49}$ Jy. We thus adopt

$$dN_{IR}/d\epsilon_{IR} = 6.3 \times 10^{10} d^2 \epsilon_{IR}^{-1.5} \tag{65}$$

J1617–5055, **J0822–4300** and **J0437–4715** There have been no available infrared or optical observations for these three pulsars. We thus simply assume that $\alpha = -1.5$ for these four pulsars and that $\nu F_\nu = 10^9$ Jy Hz at 0.01 eV. We then obtain

$$dN_{IR}/d\epsilon_{IR} = 2.5 \times 10^7 d^2 \epsilon_{IR}^{-1.5} \tag{66}$$

for J1617–5055,

$$dN_{IR}/d\epsilon_{IR} = 2.1 \times 10^7 d^2 \epsilon_{IR}^{-1.5} \tag{67}$$

for J0822–4300 and

$$dN_{IR}/d\epsilon_{IR} = 3.6 \times 10^{13} d^2 \epsilon_{IR}^{-1.5} \tag{68}$$

for J0437–4715.

4.3 Electric field structure

To reveal the spatial distribution of the acceleration field, we consider four representative boundary conditions:

    (i) case 1; $(j_1, j_2) = (0, 0)$,
    (ii) case 2; $(j_1, j_2) = (0.3, 0)$,
    (iii) case 3; $(j_1, j_2) = (0.6, 0)$,
    (iv) case 4; $(j_1, j_2) = (0, 0.3)$.

That is, for case 2 (or case 4), the positronic (or electronic) current density flowing into the gap per unit flux tube at the inner (or outer) boundary is 30 per cent of the typical Goldreich–Julian value, $\Omega/2\pi$. We fix $j_{gap} = 0.01$ for all the four cases, because the solution forms a 'brim' which disappears (fig. 2 in Hirotani & Okamoto 1998) if j_{gap} exceeds a few per cent. For example, in case 1 for $\alpha_i = 45°$, the solution for B1509–58 disappears if $j_{gap} > 0.0825$, and that for B 1951+32 disappears if $j_{gap} > 0.0968$. As typical examples of young and milli second pulsars, we consider B1509–58 and J0437–4715 to describe $E_\parallel$ distributions in the following two subsections.

4.3.1 B1509–58, a young pulsar

Since the Crab pulsar was investigated in HS01, we consider here

B1509–58 as a typical example of young pulsars. The results of $E_\parallel(s)$ for $\alpha_i = 45°$ is presented in Fig. 3. The solid, dashed, dash-dotted and dotted lines correspond to cases 1, 2, 3, and 4, respectively. The abscissa designates the distance along the last-open field line and covers the range from the neutron star surface ($s = 0$) to the position where the disance equals $s = 1.2\varpi_{LC} = 9.34 \times 10^6$ m.

The solid line shows that the gap is located around the null surface, if no currents penetrate into the gap at either of the boundaries. The gap slightly extends outwards, because the pair-production mean free path becomes small at the outer region of the gap, owing to the diluted X-ray field there. It is noteworthy that the potential drop becomes the largest when $j_1 = 0$ and $j_2 = 0$ (i.e., in case 1).

The dashed and dash-dotted lines indicate three points we may notice. For one thing, the gap shifts outwards as j_1 increases. This conclusion is consistent with the results obtained analytically and numerically in HS01. What is more, the maximum value of $E_\parallel$ decreases as the gap shifts outwards. This is because the decreased ρ_{GJ} at a larger distance reduces $|dE_\parallel/ds|$ (equation 3). One final point is that W increases as the gap shifts outwards. This is because the pair-production mean free path increases, owing to the diluted X-ray field at large radii. The potential drop in the gap remains almost unchanged between cases 2 and 3, because the decrease of maximum $E_\parallel$ and the increase of W cancel each other.

On the other hand, when j_2 increases, the gap shifts inwards. When the gap is located halfway from the null surface to the star (case 4, the dotted line), the potential drop becomes only 3 per cent of that obtained in case 1. A physical interpretation on this point is given in Section 5.1.
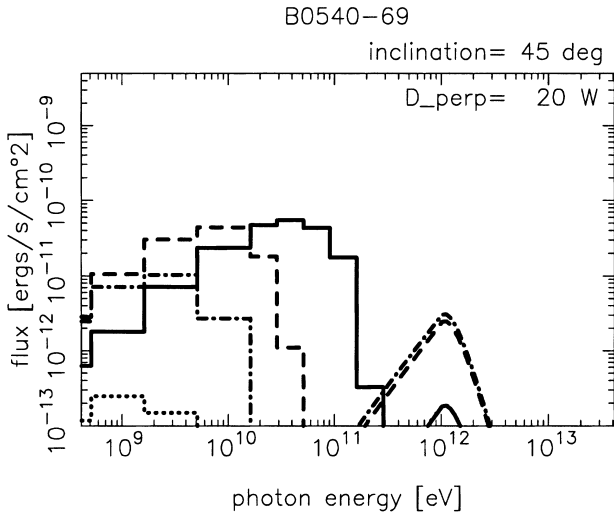
4.3.2 J0437–4715, a millisecond pulsar

We next consider J0437–4715, a millisecond pulsar. The $E_\parallel$ distribution for $\alpha_i = 45°$ is presented in Fig. 4. Even though the magnetic moment is small, the strength of $E_\parallel$ is comparable with the young pulsar B1509–58. This is because the magnetic field in the outer magnetosphere is comparable with those of young
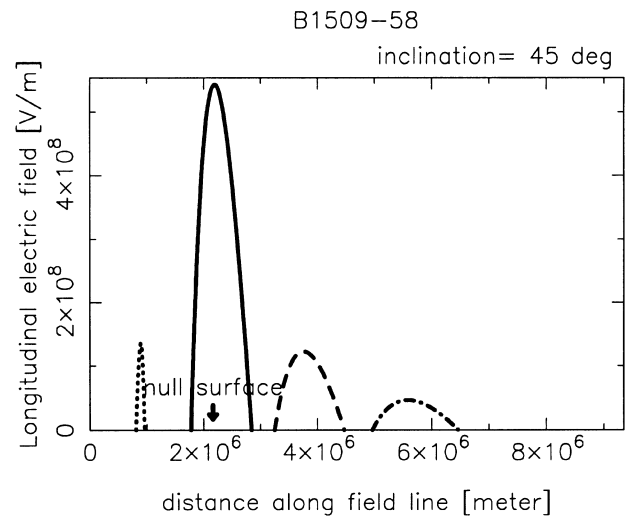
Figure 3. Distribution of the acceleration field in the magnetosphere of B1509–58, a young pulsar. The inclination angle is 45°. The abscissa is the distance from the star surface along the last-open field line. The solid, dashed, dash-dotted and dotted lines correspond to the cases 1, 2, 3 and 4, respectively (see text).
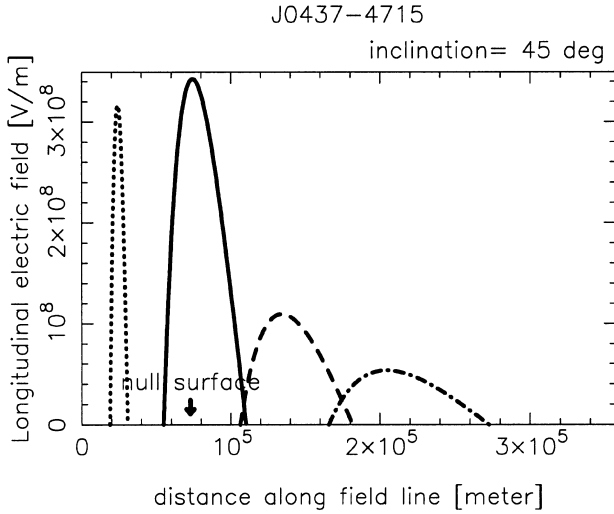
Figure 4. Distribution of the acceleration field for J0437–4715, a millisecond pulsar. The inclination angle is 45°. The abscissa, ordinate, and the lines are the same as figure Fig. 3.

Figure 6. Pulsed gamma-ray spectra from B1509–58 when $\alpha_i = 45°$. The lines correspond to the same cases as in Fig. 5.
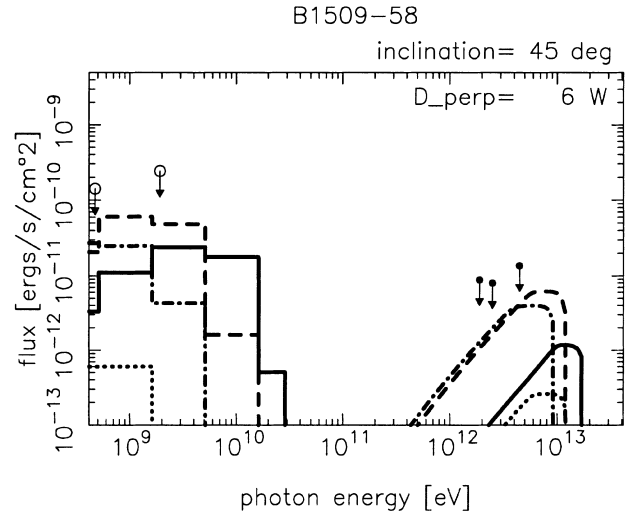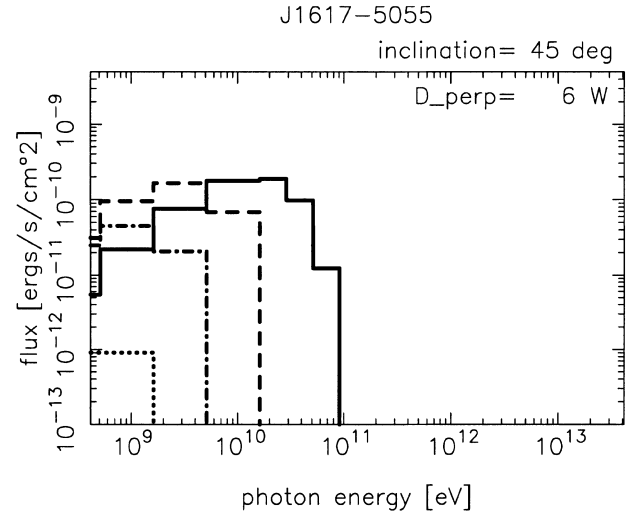

Figure 5. Pulsed gamma-ray spectra from B0540–69 magnetosphere when $\alpha_i = 45°$. The thick and thin lines denote the spectra of outwardly and inwardly propagating γ-rays, respectively. The solid, dashed, dash-dotted and dotted lines correspond to the cases 1, 2, 3 and 4, respectively (see text).

Figure 7. Pulsed gamma-ray spectra PSR J1617–30 when $\alpha_i = 45°$. The lines correspond to the same cases as in Fig. 5.

pulsars, owing to its fast rotation ($\Omega = 1092\,\mathrm{rad\,s^{-1}}$), which reduces ϖ_{LC} to 2.74×10^5 m. In addition, W is relatively close to B1509–69, a young pulsar. This is because the shrunk light cylinder of millisecond pulsars results in a dense X-ray field illuminating the gap; the dense X-ray field in turn reduces the pair-production mean free path, and hence W. This result is consistent with the semi-analytical prediction for the millisecond pulsar B1821–24 (H00b), the X-ray field of which is dominated by a power-law component. In short, the electrodynamic structures of the gap are similar between millisecond pulsars and young pulsars.

4.4 Gamma-ray spectra

The spectra of outwardly (or inwardly) propagating γ-rays in GeV energies are readily computed from $g_+^i(\xi_2)$ [or $g_-^i(\xi_1)$]. The TeV spectra, on the other hand, can be obtained by the method described

in Section 3. Except for B0540–69, the optical depth (equation 61) is much less than unity; therefore, the effect of absorption due to TeV–eV collisions in the magnetosphere can be neglected for the other six pulsars considered in this paper.

We present the combined GeV–TeV spectra for B0540–69, B1509–58, J1617–5055, J0822–4300, Vela, B1951+32 and J0437–4715, in Figs 5–12. Both the inclination angle and $D_\perp$ are indicated at the top right corner. For cases 1, 2 and 3, the spectra of outwardly propagating γ-rays are depicted as solid, dashed, and dash-dotted curves respectively, because their fluxes are greater than those of inwardly propagating ones. For case 4, we present the inwardly propagating flux as the dotted curve, because the dominant flux of the γ-rays are emitted by the inwardly migrating electrons in this case ($j_1 = 0, j_2 = 0.3$). The observed pulsed fluxes and their upper limits are indicated by open circles (data obtained by EGRET), open squares (data obtained by Whipple), open triangles (data obtained by the Durham group). The upper limits of the stationary fluxes are obtained by the CANGAROO group and are denoted by filled circles. To compare the results with the same α_i, we present the case of $\alpha_i = 45°$ for all the pulsars. For the Vela

J0822−4300

inclination= 45 deg
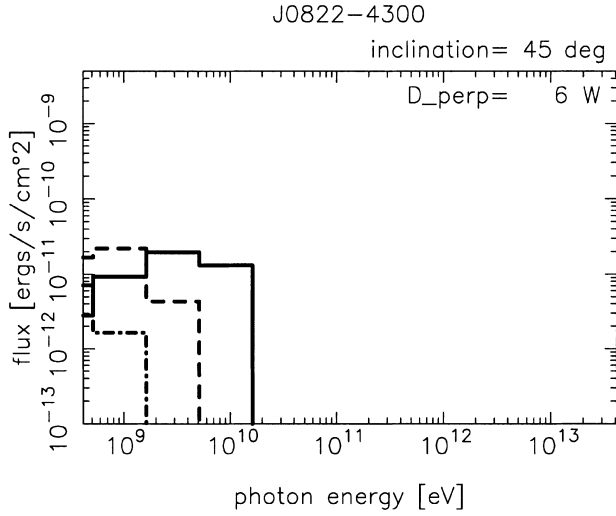
Figure 8. Pulsed gamma-ray spectra for the Vela pulsar when $\alpha_i = 45°$. The lines correspond to the same cases as in Fig. 5.

Vela

inclination= 60 deg
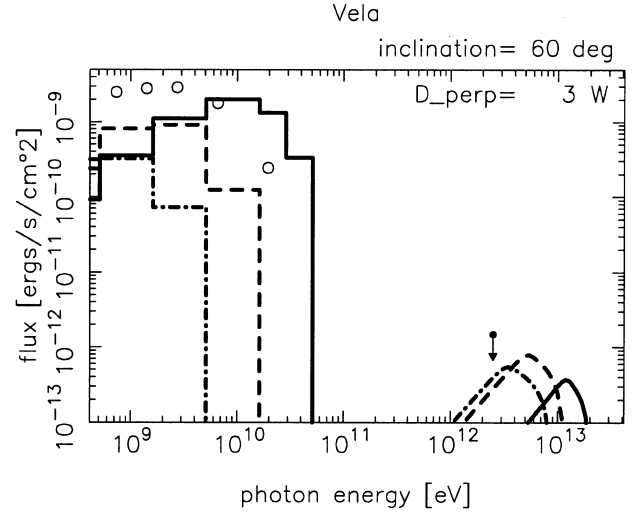
Figure 10. Pulsed gamma-ray spectra for the Vela pulsar when $\alpha_i = 60°$. The lines correspond to the same cases as in Fig. 5.

Vela

inclination= 45 deg
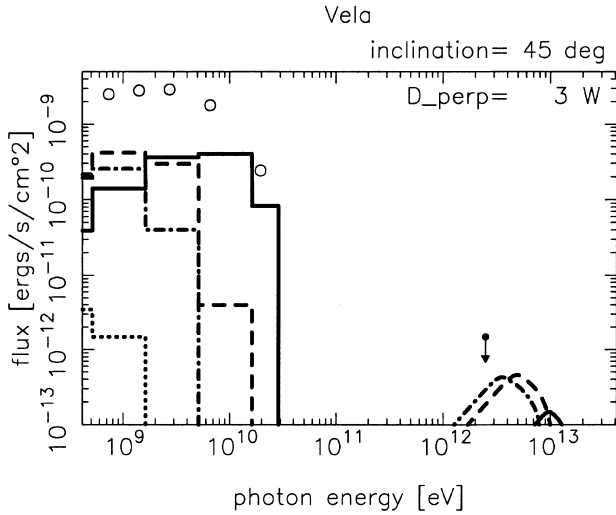
Figure 9. Pulsed gamma-ray spectra for the Vela pulsar when $\alpha_i = 45°$. The lines correspond to the same cases as in Fig. 5.

B1951+32

inclination= 45 deg
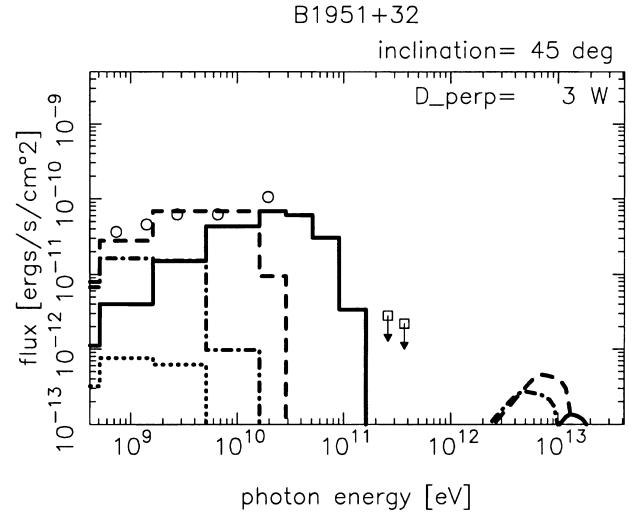
Figure 11. Pulsed gamma-ray spectra from B1951+32 when $\alpha_i = 45°$. The lines correspond to the same cases as in Fig. 5.

pulsar, we also present the case of $\alpha_i = 45°$ to examine the dependence on α_i.

4.4.1 General features

We first consider the general features of the γ-ray spectra. The GeV emission is the most luminous and hardest for case 1 (Section 4.3), because both the potential drop and the maximum of $E_\parallel$ is the largest. (see Figs 3–4). It should be noted that the larger α_i is, the harder the GeV spectrum becomes; this can be understood if we compare Figs 9 and 10. It should be noted that the same conclusion was derived independently for a vacuum gap in H00b (e.g. E_c in table 3), in which the 'gap closure' condition was considered instead of solving the stationary Vlasov equations (Section 2). Physically speaking, this is because the distance of the gap from the star decreases with increasing α_i for the same set of (j_{gap}, j_1, j_2). At small radii, the strong magnetic field enlarges ρ_{GJ}, and hence $|dE_\parallel/ds|$, which results in a large $E_\parallel$ at the gap centre, especially when the gap is nearly vacuum (as the solid lines indicate in Fig. 11).

We can also understand that the TeV fluxes are generally kept below the observational upper limits for appropriate GeV fluxes, or equivalently, appropriate cross-sectional area, $D_\perp^2$. Therefore, the problem of the excessive TeV flux does not arise for reasonable IR densities of individual pulsars. If the (unobserved) IR flux is absorbed below optical wavelength due to synchrotron self-absorption, the upscattered, TeV flux decreases from the predicted values presented in Figs (5–12). In the next subsection, we consider the expected spectra source by source.

4.4.2 Comparison with EGRET observations

First, we consider the Vela pulsar. It follows from Figs 9 and 10 that the pulsed GeV spectrum obtained by EGRET (Kanbach et al. 1994; Fierro et al. 1998) is impossible to be explained if the gap is located well inside of the null surface, as the dotted lines indicate. A large inclination angle and small current inflows are preferable to explain the observed flux above TeV. For $\alpha_i > 45°$, the expected TeV fluxes are well below the observed upper limit (Yoshikoshi et al. 1997).
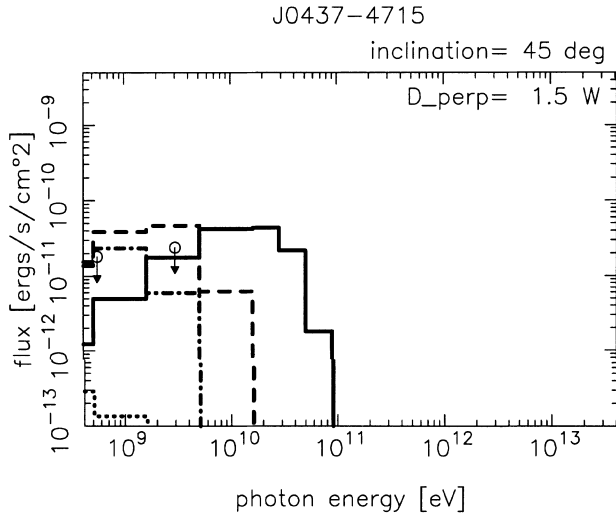
J0437−4715

Figure 12. Pulsed gamma-ray spectra for J0437–4715 when $\alpha_i = 45°$. The lines correspond to the same cases as in Fig. 5.
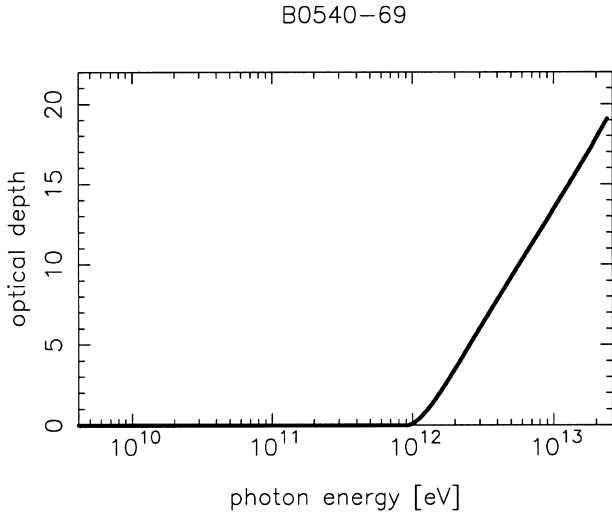
B0540−69

Figure 13. Pair-production optical depth for a TeV photon to be absorbed in the homogeneous, isotropic IR field in the magnetosphere of pulsar B0540–69. The abscissa designates the γ-ray frequency.

Secondly, we consider B1951+32. It follows again that the observed GeV flux around 10 GeV (Ramanamurthy et al. 1995) is impossible to be emitted if the gap is located well inside of the null surface, as the dotted lines indicate. The expected TeV flux is much less than the observed upper limits (Srinivanan et al. 1997).

Finally, we consider the other pulsars whose GeV fluxes were not detected by EGRET. For B0540–69, the basic properties are common with the Crab pulsar (HS01) as follows.

(i) $W \ll \varpi_{LC}$ holds because of its large X-ray density.

(ii) The intrinsic TeV flux is comparable or even somewhat greater than the GeV flux but is significantly absorbed by its dense, magnetospheric IR field. For example, in case 1, the intrinsic TeV flux before absorption attains 1.7×10^{13} Jy Hz at 1.4×10^{27} Hz, which is about two times greater than the maximum of the GeV flux. In Fig. 13, we present the absorption optical depth (equation 61). The resultant, absorbed TeV spectra are depicted in Fig. 5, together with the GeV spectra.

(iii) The curvature spectra are relatively hard (fig. 5), because its strong magnetic field at the gap increases $E_{\parallel}$, although its W is small.

For B1509–58, its relatively less dense IR field (compared with Crab and B0540–69) cannot absorb enough TeV flux in the magnetosphere. As a result, the expected TeV flux becomes comparable with the observational upper limit while the GeV flux is well below the observational upper limits (fig. 6).

In the case of J1617–5055, its GeV spectrum (fig. 7) is softer than Crab (HS01) and B0540–69, because its X-ray field is less dense compared with these two young pulsars. Its TeV flux is small because of its small IR field assumed (Section 3.1).

The GeV spectrum of J0822–4300 (fig. 8) is softer than that of Vela, although the X-ray field more or less similar each other. This is because the former's high-temperature surface emission provides a denser X-ray field, which shrinks the pair-production mean free path, and hence W to reduce $E_{\parallel}$, compared with Vela.

For J0437–4715, the GeV flux is large (fig. 12), although we assume a small cross-sectional area, $D_{\perp}^2 = (1.5W)^2$. This large Gev flux comes from the fact that millisecond pulsars have similar electrodynamic structure with young pulsars. Compared with the EGRET upper limit of pulsed emissions (Thompson 2000), we can expect that this milli-second pulsar is an attractive target for the next-generation GeV telescopes.

5 DISCUSSION

In summary, we have developed a one-dimensional model for an outer-gap accelerator in the magnetosphere of a rotating neutron star. When the particles penetrate into the gap from the inner (or outer) boundary, the gap shifts outwards (or inwards). Applying the theory to Vela and B1951+32, we find that the GeV spectrum softens significantly and cannot explain the EGRET observations, if the gap is located well inside of the null surface. We can therefore conclude the gap should be located near to or outside of the null surface for these two pulsars. We also apply the theory to B0540–69, B1509–58, J1617–5055, J0822–4300, and J0437–4715 and find that the TeV fluxes are undetectable by current ground-based telescopes for moderate cross-sectional areas of the gap for all the seven pulsars mentioned just above, if we estimate their magnetospheric IR field by interpolating radio and optical pulsed fluxes. For B0540–69, its intrinsically large TeV flux is absorbed by its dense IR field to become undetectable; this conclusion is analogous with what was obtained in HS01 for the Crab pulsar.

5.1 Gap-closure condition

In Section 4.3.1, we pointed out that the potential drop decreases significantly as the gap shifts inwards from the null surface. In this subsection, we interpret this behaviour from the gap-closure condition investigated in H00a and Hoob. In a stationary gap, the pair production optical depth, W/λ_p, equals the ratio $N_\gamma(j_{gap}/j_{tot})$, where λ_p and N_γ refer to the pair-production mean free path and the number of γ-rays emitted by a single particle, respectively. We thus obtain the following gap closure condition:

$$W = \lambda_p N_\gamma \frac{j_{gap}}{j_{tot}}. \tag{69}$$

This condition is automatically satisfied by the stationarity of the Boltzmann equations. For example, consider the case when the external current is 10 times greater than the one created in the gap. In this case, the expectation value for the γ-rays that are emitted from a single particle in the gap should be one-tenth so that a

stationary pair-production cascade may be maintained, because not only the produced particles but also the externally injected particles emit γ-rays in the same way.

As the gap shifts inwards, the X-ray density increases to reduce λ_p. At the same time, the ratio j_{gap}/j_{tot} decreases as j_2 increases. As a result, W decreases very rapidly with increasing j_2. Owing to the rapidly decreasing W, the integrated potential drop significantly decreases, although the local ρ_{GJ}, and hence $|dE_\parallel/ds|$, increases inwards.

If the gap shifts outwards, on the other hand, the increase of λ_p and the decrease of j_{gap}/j_{tot} partially cancel each other. As a result, the potential drop decreases only slightly with increasing j_1.

5.2 Comparison with ZC97

It is worth comparing the present method with ZC97, who considered that the gap size is limited so that the emitted γ-rays may have energies just above the pair-production threshold in collisions with the surface X-rays that are caused by the bombardment of produced particles in the gap. Their method qualitatively agrees with the current gap closure condition (equation 69), provided $j_{gap}/j_{tot} \sim 1$ (see Section 5.8 in H00b); case 1 ($j_1 = j_2 = 0$) corresponds to this case. However, as j_2 increases, the factor ($j_{gap}j_{tot}$) in equation (69) becomes small to reduce W. In other words, the closure condition adopted by ZC97 would become inconsistent with stationary Vlasov equations (Section 2), if we were to overextraporate it to the case when $j_2 \sim 1$. In the same manner, we cannot overextraporate the gap-closure condition of ZC97 to the case when j_1 increases and hence the gap shifts towards the light cylinder (as cases 2 and 3), because j_{gap}/j_{tot} decreases substantially.

5.3 Inverse compton scatterings in the young pulsar magnetosphere

Although the dense IR field of young pulsars (B0540–69, B1509–58) results in a relatively large intrinsic TeV emission compared with other pulsars, the intrinsic TeV flux is not more than the GeV flux, provided $\alpha_i > 45°$. Therefore, the radiation reaction force is caused primarily by the curvature process rather than the inverse Compton scatterings, as long as j_2 is less than 0.3. However, if j_2 exceeds 0.3, we cannot in general rule out the possibility of the case when the radiation reaction is caused by IC scatterings. This is because the dense X-ray field will suppress the particle Lorentz factors (Paper II) below 10^7, and because such less-energetic particles scatter copious IR photons into lower γ-ray energies with large cross-sections ($\sim \sigma_T$). As a result, the GeV emissions may be mainly due to IC scattering in this case. Moreover, as the magnetic field becomes very strong close to the star, not only the synchro-curvature process (ZC97), but also a magnetic pair production becomes important. There is room for further investigation of the case when an 'outer' gap is located close to the polar cap.

ACKNOWLEDGMENTS

REFERENCES

Aschenbach B., Brinkmann W., 1975, A&A, 41, 147
Becker W., Truümper J., 1993, Nat, 365, 528
Berestetskii V. B., Lifshitz E. M., Pitaevskii L. P., 1989, Quantum Electrodynamics, 3rd edn.
Beskin V. S., Istomin Ya. N., Par'ev V. I., 1992, SvA, 36, 642
Blumenthal G. R., Gould R. J., 1970, Rev. Mod. Phys., 42, 237
Caraveo P. A., Mereghetti S., Bignami G. F., 1994, ApJ, 423, L125
Caraveo P. A., Bignami G. F., Mignani R., Taff L. G., 1996, ApJ, 461, L91
Cheng K. S., 1994, Towards a Major Atmospheric Cerenkov Detector III. Universal Academy Press, p. 25
Cheng K. S., Ho C., Ruderman M., 1986a, ApJ, 300, 500 (CHR)
Cheng K. S., Ho C., Ruderman M., 1986b, ApJ, 300, 522 (CHR)
Cheng K. S., Ruderman M., Zhang L., 2000, ApJ, 537, 964
Chiang J., Romani R. W., 1992, ApJ, 400, 629
Chiang J., Romani R. W., 1994, ApJ, 436, 754
Daishido T., 1975, PASJ, 27, 181
Daugherty J. K., Harding A. K., 1982, ApJ, 252, 337
Daugherty J. K., Harding A. K., 1996, ApJ, 458, 278
Dermer C. D., Sturner S. J., 1994, ApJ, 420, L75
Downs G. S., Reichley P. E., Morris G. A., 1973, ApJ, 181, L143
Edwards P. G. et al., 1994, A&A, 291, 468
El-Gowhari A., Arponen J., 1972, Nuovo Cimento, 11B, 201
Fierro J. M., Michelson P. F., Nolan P. L., Thompson D. J., 1998, ApJ, 494, 734
Gil J. A., Krawczyk A., 1996, MNRAS, 285, 561
Greenstein G., Hartke G. J., 1983, ApJ, 271, 283
Halpern J. P., Martin C., Marshall H. L., 1996, ApJ, 462, 908
Halpern J. P., Wang Y. H., 1997, ApJ, 477, 905
Hardee P. E., Rose W. K., 1974, ApJ, 194, L35
Harding A. K., Tademaru E., Esposito L. S., 1978, ApJ, 225, 226
Hirotani K., 2000a, MNRAS, 317, 225 (H00a)
Hirotani K., 2000b, ApJ, 549, 495 (H00b)
Hirotani K., 2000c, PASJ, 52, 1 (H00c)
Hirotani K., Okamoto I., 1998, ApJ, 497, 563
Hirotani K., Shibata S., 1999a, MNRAS, 308, 54 (Paper I)
Hirotani K., Shibata S., 1999b, MNRAS, 308, 67 (Paper II)
Hirotani K., Shibata S., 1999c, PASJ, 51, 683 (HS99)
Hirotani K., Shibata S., 2001, submitted to ApJ (HS01)
Kanbach G. et al., 1994, A&A, 289, 855
Kaspi V. M., Lackey J. R., Manchester R. N., Bailes M., Pace R., 2000, ApJ, 528, 445
Kawai N., Okayasu R., Sekimoto Y., 1993, in Friedlander M., Gehrels N., Macomb D. J., eds, AIP Conf. Proc. 280, Compton Gamma-Ray Observatory. Am. Inst. Phys., New York, p. 213
Kifune T., 1996, Space Sci. Rev., 75, 31
Krause-Polstorff J., Michel F. C., 1985a, MNRAS, 213, 43
Krause-Polstorff J., Michel F. C., 1985b, A&A, 144, 72
Kundt W., Schaaf R., 1993, Ap&SS, 200, 251
Manchester R. N., Wallace P. T., Peterson B. A., Elliott K. H., 1980, MNRAS, 190, 9, P
Manchester R. N., Mar D. P., Lyne A. G., Kaspi V. M., Johnston S., 1993, ApJ, 403, L29
Mayer-Hasselwander H. A., Bertsch D. L., Brazier T. S., Chiang J., Fichtel C. E., Fierro J. M., Hartman R. C., Hunter S. D., 1994, ApJ, 421, 276
Middleditch J., Pennypacker C., 1985, Nat, 313, 659
Michel F. C., 1974, ApJ, 192, 713
Nel H. I., De Jager O. C., Raubenheimer B. C., Brink C., Meintjes P. J., Nortt A. R., 1993, ApJ, 418, 836
Nolan P. L. et al., 1993, ApJ, 409, 697
Ochelkov Yu. P., Usov V. V., 1980a, Ap&SS, 69, 439
Ochelkov Yu. P., Usov V. V., 1980b, Sov. Astron. Lett. (USA), 6, 414
Oügelman H., Finley J. P., Zimmermann H. U., 1993, Nat, 361, 136
Pavlov G. G., Shibanov Yu. A., Ventura J., Zavlin V. E., 1994, A&A, 289, 837
Petre R., Becker C. M., Winkler P. F., 1996, ApJ, 465, L43

Ramanamurthy P. V. et al., 1995, ApJ, 447, L109

Reynoso E. M., Dubner G. M., Goss W. M., Arnal E. M., 1995, AJ, 110, 318

Romani R. W., 1987, ApJ, 313, 718

Romani R. W., 1996, ApJ, 470, 469

Romani R. W., Yadigaroglu I. A., 1995, ApJ, 438, 314

Rybicki G. B., Lightman A. P., 1979, Radiative processes in astrophysics. Wiley, New York

Safi-Harb S., Oügelman H., Finley J. P., 1995, ApJ, 439, 722

Saito Y., 1998, PhD thesis, Univ. Tokyo

Sandhu J. S. et al., 1997, ApJ, 478, L95

Seward F. D., Harnden F. R., Szymkowiak A., Swank J., 1984, ApJ, 281, 650

Shibanov Yu. A., Zavlin V. E., Pavlov G. G., Ventura J., 1992, A&A, 266, 313

Shibata S., 1995, MNRAS, 276, 537

Shibata S., Miyazaki J., Takahara F., 1998, MNRAS, 295, L53

Srinivanan R. et al., 1997, ApJ, 489, 170

Sturner S. J., Dermer C. D., Michel F. C., 1995, ApJ, 445, 736

Taylor J. H., Manchester R. N., Lyne A. G., 1993, ApJS, 88, 529

Thompson D. J., 2000, Adv. Space Res., 25, 659

Thompson D. J., Bailes M., Bertsch D. L., Esposito J. A., Fichtel C. E., Harding A. K., Hartman R. C., Hunter S. D., 1996, ApJ, 465, 385

Thompson D. J. et al., 1999, ApJ, 516, 297

Torii K. et al., 1998, ApJ, 494, L207

Usov V. V., 1994, ApJ, 427, 394

Yoshikoshi T., Kifune T., Dazeley S. A., Edwards P. G., Hara T., Hayami Y., Kakimoto F., Konishi T., 1997, ApJ, 487, L65

Zavlin V. E., Pavlov G. G., Shibanov Yu. A., Ventura J., 1995a, A&A, 297, 441

Zavlin V. E., Shibanov Yu. A., Pavlov G. G., 1995b, Astron. Lett., 21, 149

Zavlin V. E., Pavlov G. G., 1998, A&A, 329, 583

Zhang L., Cheng K. S., 1997, ApJ, 487, 370 (ZC97)

This paper has been typeset from a TeX/LaTeX file prepared by the author.